


Cite this: *Nanoscale Adv.*, 2024, 6,
3887

Methylene blue removal using a nanomagnetic support: a response surface approach†

Thais Ribeiro do Nascimento Moraes Calazans,^a Ana Carolina de Lima Barizão,^b Thais de Andrade Silva,^a Fabiana Vasconcelos Campos,^a Sérgio Tulio Alves Cassini,^b Araceli Veronica Flores Nardy Ribeiro,^c Madson de Godoi Pereira,^d Marco Cesar Cunegundes Guimarães,^a Jairo Pinto de Oliveira ^{*ab} and Joselito Nardy Ribeiro^a

Textile wastewater is commonly released into water bodies without appropriated treatment, resulting in environmental damages. Processes involving separation and adsorption using nanomagnetic supports have been considered a promising alternative to address this concern. However, challenges concerning the low stability of nanoparticles and the reproducibility of experiments make their large-scale application difficult. In this study, we evaluated the efficiency of methylene blue (MB) removal by Fe₃O₄ nanoparticles coated with sodium dodecyl sulfate (MNP-SDS). The nanomaterial was characterized by transmission electron microscopy (TEM), X-ray diffraction (XRD), Raman spectroscopy, and Fourier-transform infrared spectroscopy (FTIR). The adsorption process was optimized in two stages using factorial design. In the first stage the most influential variables (reaction time, temperature, agitation, pH, and dye concentration) were selected based on the existing literature and applied in a fractional factorial (2⁽⁵⁻¹⁾). In the second stage, the main variables identified were used in a complete factorial (3²). The highest removal percentage was obtained using 15 g L⁻¹ of MNP-SDS, which led to a q_{exp} of 1.5 mg g⁻¹. Isothermal analysis parameters and a negative Gibbs free energy indicate that the process was spontaneous, favorable, and that the data were best fitted to the Langmuir model.

Received 17th April 2024
Accepted 8th June 2024

DOI: 10.1039/d4na00318g

rsc.li/nanoscale-advances

Introduction

Methylene blue (MB) is an organic chloride salt commonly applied in the wood, silk, and linen processing industries.¹ Despite its importance, it can also be highly toxic, potentially leading to severe skin irritation, burns, respiratory failure, and even cancer.^{1,2} Because of its chemical structure, which consists of aromatic rings, MB exhibits high stability and resistance to both photo and thermal degradation. Thus, its removal from industrial wastewater has been the goal of several studies.^{3,4} Processes such as coagulation and flocculation,⁵ ozonation,⁶ electrochemical degradation,⁷ and filtration⁸ have been considered. However, issues such as high complexity and cost can render them unfeasible.⁹

Adsorption is another example of a pollutant removal technique characterized by high performance, even when applied to low concentrations of pollutants. In general, the process

involves the transfer of the mass of molecules present in a liquid or gaseous medium (adsorbate) to the surface of a solid (adsorbent).¹⁰ Different materials can be used as adsorbents, varying both in composition polymers, metals, carbon materials and others¹¹⁻¹³ and structure nanoparticles, nanotubes, gels, foams, membranes, films and others.¹⁴⁻¹⁷ The properties of the adsorbent such as surface area, porosity, active sites available on the surface of the adsorbent, surface charge and others are directly related to the performance of the adsorption process.¹⁸ Therefore, proper consideration of these characteristics and their relationship with the adsorbate can result in the separation of contaminants with a high degree of efficiency. A good example is the study carried out by El-Desouky *et al.*,¹⁹ where they obtained an adsorption capacity of tartrazine in aqueous solution of 710.75 mg g⁻¹ using an organic framework alginate air-gel composite sponge as adsorbent, while Alsawat²⁰ synthesized a CuSnO₂TiO₂ nanocomposite that showed a high adsorption capacity for Congo red dye, presenting a maximum adsorption capacity of 277 mg g⁻¹.

In general, magnetic nanoparticles stand out as excellent adsorbents. They typically offer high adsorption performance, mainly due to their large surface area, in addition to low cost and potential for reuse.⁹ However, the agglomeration phenomenon can effectively reduce the magnetism of MNPs,

^aFederal University of Espírito Santo, Vitória, Espírito Santo 29075-910, Brazil. E-mail: jairo.oliveira@ufes.br

^bCenter for Research, Innovation and Development of Espírito Santo, CPID, Brazil

^cFederal Institute of Espírito Santo-IFES, Vila Velha-ES, Brazil

^dState University of Bahia, Salvador, BA 41150-000, Brazil

† Electronic supplementary information (ESI) available. See DOI: <https://doi.org/10.1039/d4na00318g>



creating a bottleneck in the application of this technique. A highly effective solution to circumvent this issue is the functionalization of nanoparticles with molecules such as inorganic acids, surfactants, and polymers.^{9,21} Surfactants are often described in the literature as barriers that not only prevent agglomeration but also modify the surface charge of MNPs.^{21,22} Sodium dodecyl sulfate (SDS), for instance, is an anionic surfactant²³ capable of interacting with Fe₃O₄ nanoparticles, resulting in highly negative nanoparticles that can interact with the positive charges present on the surface of certain compounds, such as MB.²⁴

Although the outcome is usually satisfactory, the large number of variables involved in the process can interfere with adsorption efficiency.²⁵ In this scenario, factorial design experiments are an important asset, owing to their simplicity, reduced number of experiments, and the ability to simultaneously investigate multiple factors, allowing for the assessment of the relevance and statistical significance of the variables under study. Fractional factorial design is crucial in initial optimization steps, while the full factorial approach (second order; *e.g.*, central composite design) can polish the results by combining levels of factors.²⁶

In the present study, we synthesized iron oxide nanoparticles and functionalized them with SDS, aiming to address MB removal. The NPs were characterized using TEM, XRD, Raman spectroscopy, and FTIR spectroscopy. The efficiency of MB removal was first analyzed using a fractional factorial ($2^{(5-1)}$), in which the range of variables used (time, temperature, pH, agitation, and concentration of reagents) was based on a thorough literature review. The most significant variables were optimized by a full factorial design experiment (3^2). In addition, the affinity between functionalized nanoparticles and MB and the maximum adsorption capacity were investigated through isothermal experiments, by fitting the data to the Langmuir and Freundlich models. Information on the spontaneity of the process was obtained through the calculation of the Gibbs free energy variation (ΔG°). Our results contribute to the comprehension of the adsorption process using nanomagnetic supports and experiment optimization, paving the way for future industrial-scale applications.

Methods

Materials

FeCl₂·4H₂O (Sigma-Aldrich 44939), FeCl₃·6H₂O (Sigma-Aldrich F2877), ammonium hydroxide (Proquimios), sodium hydroxide (Neon 1824), hydrochloric acid (Neon 1789), sodium dodecyl sulfate (Sigma-Aldrich, L5750), methylene blue (Neon, L44107), Argon (99.99%, White Martins, Brazil), and ultrapure water (Millipore, Synergy UV).

Synthesis, functionalization, and characterization of magnetic nanoparticles

MNPs were synthesized by the chemical coprecipitation method. In a volumetric flask, 40 mL of 0.09 M FeCl₂·4H₂O and 40 mL of 0.18 M FeCl₃·6H₂O were combined. After complete salt

dissolution, 7.5 mL of NH₄OH (28%) was added at a flow rate of 5 mL min⁻¹, under constant stirring, for 10 min at 65 °C, resulting in a black precipitate (Fe₃O₄). At this stage, the reaction was placed in an ice bath for immediate interruption. The resulting nanoparticles were washed three times with ultrapure water and functionalized using 2% SDS (CH₃(CH₂)₁₁SO₄Na), by stirring them together for 15 min at 25 °C under constant agitation (150 rpm). The functionalized nanoparticles (MNP-SDS) were washed three times for removing unreacted SDS, resuspended in ultrapure water, and stored at 8 °C. The nano-material was characterized by transmission electron microscopy (TEM), X-ray diffraction (XRD), Raman spectroscopy, and Fourier-transform infrared spectroscopy (FTIR).

Factorial design

On account of the wide range of variables involved in the adsorption process, we carried out a preliminary screening of the most influent variables by applying a fractional factorial design $2^{(5-1)}$. The variables were selected based on a comprehensive literature review (Tables S1 and S2 ESI†). Following this screening, a full factorial design (3^2) was conducted, in order to optimize the process and determine the best experimental conditions for MB removal. Tables 1 and 2 present the simplified matrix of the fractional factorial design $2^{(5-1)}$ and that of the complete factorial design (3^2), respectively. Detailed matrices for the fractional and complete factorial designs can be found in the ESI (Tables S3 and S4).†

Experiments were carried out in an orbital shaker, using 10 mL of MB dye (20 mg L⁻¹) and 1 mL of MNP-SDS. At the end of the reaction time, the solution was exposed to a magnetic field for 15 min and the concentration of MB in the supernatant determined by UV-vis spectrophotometry (685 nm).

Adsorption study

Following the optimization step, the adsorption curve experiments were conducted with the variables and levels fixed as such: reaction time, 32.2 min; temperature, 22.6 °C; agitation, 150 rpm; pH 5; and dye concentration, 25 mg L⁻¹. The assays were performed in an orbital shaker, MNP-SDS concentrations varying from 0 to 50 mg L⁻¹. After defining the optimal concentration of MNP-SDS (15 mg L⁻¹), adsorption isothermal experiments were carried out to determine the maximum adsorptive capacity.

Table 1 Simplified matrix of the fractional factor design $2^{(5-1)}$

Variable	Min. level (-)	Max. level (+)
Time (min)	1	20
Temperature (°C)	25	45
pH	5	9
Adsorbent mass (mg)	5	25
Agitation (rpm)	100	300



Table 2 Simplified matrix of the complete factorial design (3²)

Variable	Min. level (−)	(0)	Max. level (+)
Time (min)	1	31	61
Temperature (°C)	20	30	40

$$\Delta G^\circ = -RT \ln K \quad (3)$$

In which R is the ideal gas constant ($8.3144 \text{ J K}^{-1} \text{ mol}^{-1}$), T is the temperature in Kelvin, and K is the equilibrium constant.²⁷

Results and discussion

Synthesis and characterization of nanoparticles

Isothermal and thermodynamic parameters

Adsorption isothermal experiments were performed using different MB concentrations ($5\text{--}400 \text{ mg L}^{-1}$), whereas the other variables were set at their optimal values. NP-SDS and MB were incubated for 32.2 min under constant stirring at $22.6 \text{ }^\circ\text{C}$. At the end of the reaction time, the solution was exposed to a magnetic field for 15 min and the concentration of MB in the supernatant determined by UV-vis spectrophotometry (685 nm). The results were fitted with two different isothermal models, Langmuir and Freundlich (eqn (1) and (2), respectively), in order to identify adsorption behavior.

$$q = K_F C_e^{1/n} \quad (1)$$

$$q = q_{\max} K_L C_e / (1 + K_L C_e) \quad (2)$$

In which q is the amount of solute adsorbed per gram of adsorbent at equilibrium (mg g^{-1}), q_{\max} is the maximum adsorption capacity (mg g^{-1}), K_L and K_F are the Langmuir and Freundlich adsorption capacity constants (mg L^{-1}), which reflect the interaction between adsorbate and adsorbent, C_e is the concentration of adsorbate at equilibrium (mg L^{-1}), and $1/n$ is related to surface heterogeneity. Regarding thermodynamic parameters, the Gibbs free energy variation ΔG° was calculated as follows (eqn (3)).²⁷

The magnetic iron oxide nanoparticles were synthesized through the chemical precipitation of $\text{Fe}^{2+}/\text{Fe}^{3+}$ ions in an alkaline medium and inert argon atmosphere. A black precipitate was observed at the end of the reaction, with magnetic properties becoming apparent upon the application of an external magnetic field. The UV/visible absorption spectrum for the MNPs is shown in Fig. 1A. A broader band can be observed in the ultraviolet region ($300\text{--}400 \text{ nm}$), reflecting the surface Plasmon resonance of iron oxide NPs.²⁸ Isolated particles had an absorption peak at 210 nm , which is typical of magnetite (Fe_3O_4).²⁹

The analysis performed by DLS revealed an average hydrodynamic particle size of 200 nm , possibly due to the hydration layer adhered to the metallic surface (Fig. 1C). The zeta potential of -40 mV indicates high chemical stability, which is attributed to the OH groups adhered to the metallic surface. X-ray diffraction analysis determined the crystallite structure of the MNP-SDS (Fig. 1B). Five characteristic diffraction peaks were observed, (220), (311), (400), (440), (511), which correspond to the inverse spinel structure of the magnetite.³⁰ Peaks at (113) and (210), corresponding to goethite and maghemite, were not detected, thus confirming the purity of the sample.³¹ The nanomagnetite showed excellent magnetic property (Fig. 1D and E). TEM images of the MNPs revealed the predominance of spherical nanoparticles, which was confirmed by an aspect ratio

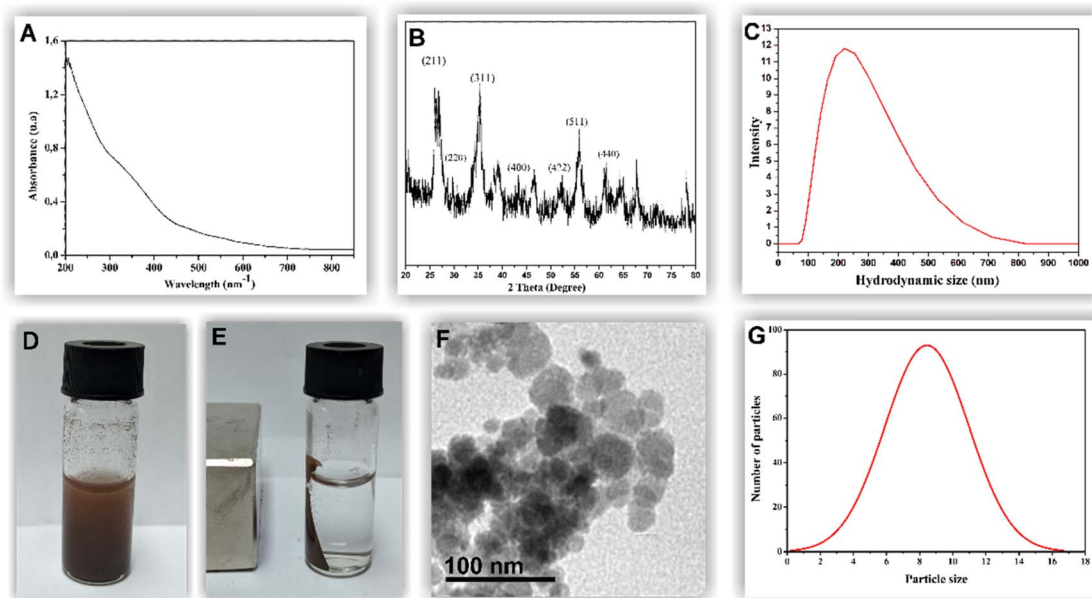


Fig. 1 UV-vis spectrum (A) and XRD of Fe_3O_4 particles (B). Histogram obtained by DLS (C). Nanomagnetite supports suspended in the solution (D). Nanomagnetite supports attracted by a magnetic field (E). Image of Fe_3O_4 MNPs by TEM (F). Histogram of the size distribution of MNPs obtained by TEM. (G).



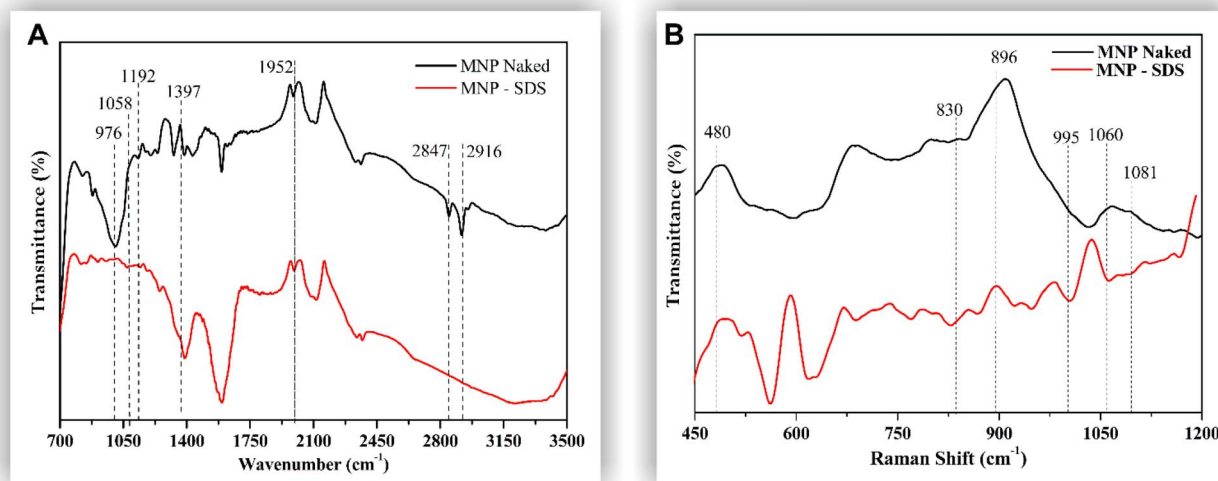


Fig. 2 FTIR (A) and Raman (B) spectra of naked Fe₃O₄ NPs and nanoparticles functionalized with SDS (MNP-SDS).

of 0.96 ± 0.30 . On average, the nanoparticles analyzed measured 8.44 ± 2.54 nm in size (Fig. 1F and G).

The MNPs were functionalized with SDS according to the protocol described in the methods section. To evaluate the interaction of this surfactant with the metallic surface, functionalized MNPs were evaluated by FTIR and Raman spectroscopy. A wide band in the 3000–3500 cm⁻¹ range was observed in the FTIR spectrum (Fig. 2A). This band is characteristic of O–H bonds, with resonance at 1952 cm⁻¹, possibly due to the vibration of the oxygen atom.³² The bands observed in the 1000–1400 cm⁻¹ range of the MNP-SDS spectrum are related to the SO₂ and SO groups of sulfur compounds, which usually produce strong infrared bands in this region due to S=O stretching, thus indicating the success of the functionalization process.^{32–34} The bands around 2916 and 2847 cm⁻¹, observed in the MNP-SDS spectrum, are assigned to C–H stretching vibrations, also

confirming presence of SDS.³⁵ The Raman scattering spectra (Fig. 2B) showed vibrations at 480 cm⁻¹ that are related to Fe–O interactions.³⁶ The 830 cm⁻¹ band reflects CO–SO₃ stretching vibrations. The peak at 896 cm⁻¹ is attributed to the C–C single bond.^{37,38} The 995 cm⁻¹ band is attributed to the stretching vibration of S–OC.³⁹ The 1060 cm⁻¹ and 1,081 cm⁻¹ bands are assigned to the full-reflex vibration and a twist mode of the C–C bond, respectively, and both may be mixed with SO₃ vibrations. The aforementioned results strongly suggest that SDS has adhered to the metallic surface of the nanoparticles.

Factorial design results

A thorough literature review was carried out to determine which variables and levels are most important for the removal of methylene blue with MNP-SDS (Tables S1 and S2 of the ESI†). As many variables can affect the removal process, we used the 2^(5–1)

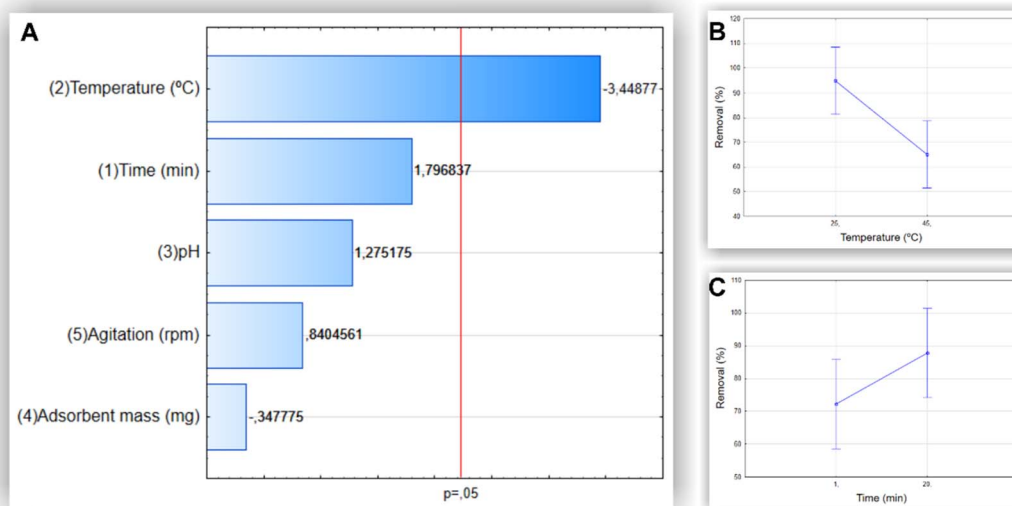


Fig. 3 Pareto charts indicate the effect of variables in the MB removal process (%) (A). Bars that surpass the vertical line indicate that the parameters are significant ($p < 0.05$). Individual influences of the variables temperature (B) and time (C) on MB removal (%).



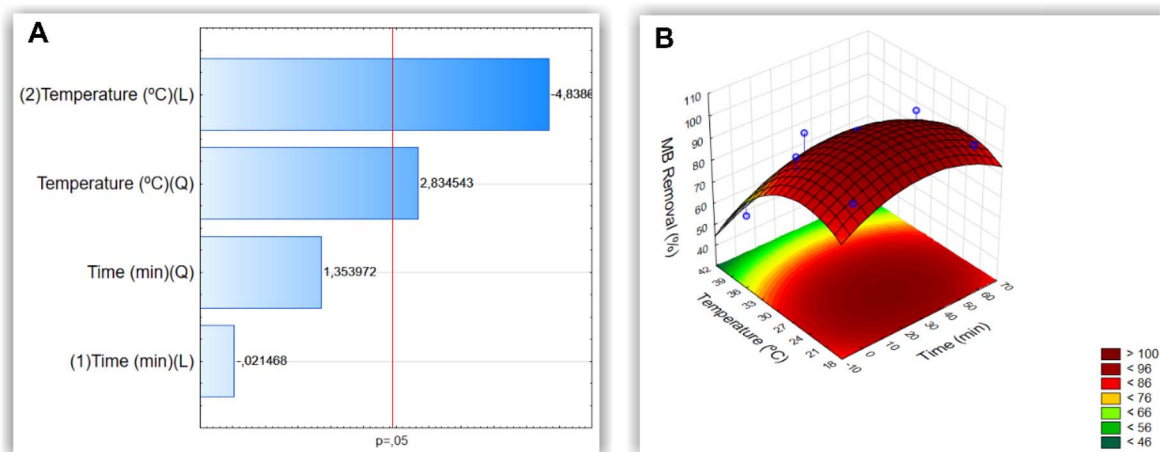


Fig. 4 Pareto chart indicates the effect of the variables analyzed in the MB removal process (%) (A). Bars that surpass the vertical line indicate that the parameters are significant ($p < 0.05$). Surface response plot of MB removal (%) (B).

fractional factorial design to select the most significant ones (p value < 0.05), considering removal percentage ($R\%$) as response variable. As can be observed in the Pareto charts (Fig. 3), time and temperature were the most influent variables in the MB removal process, although time did not reach significance. Therefore, these variables were selected for the optimization process in a full factorial design. We observed an increase in $R\%$ as a function of the decrease in temperature and increase in time.

A complete experimental factorial design (3^2) with three levels and two factors (time and temperature) was used to optimize the experimental conditions for methylene blue removal. The analyses of the individual and combined effects of the variables evaluated are presented in the Pareto chart and surface response plot shown in Fig. 4A and B, respectively. The Pareto chart confirms that temperature was the most influential variable in the process. The surface response plot reveals the

optimal interaction point between temperature and time, enabling the attainment of the optimal reaction conditions.

Characterization of MNP-SDS–methylene blue

The adsorption of methylene blue on the surface of the MNP-SDS was assessed through FTIR (Fig. 5A) and Raman (Fig. 5B) spectroscopy. The FTIR analysis shows the out-of-plane bending vibrations of the ring's C–H at 861 cm^{-1} . A C–S–C vibration was detected at 1064 cm^{-1} and the –C–N stretching absorption peak at 1252 cm^{-1} . Stretching vibrations of the –CH₂ or –CH₃ groups can be found from 1400 cm^{-1} to 1300 cm^{-1} . A band that extends from 1400 to 1500 cm^{-1} corresponds to C=C side ring stretching. A vibration of the CH=N bond was identified at 1600 cm^{-1} .⁴⁰ The Raman spectrum (Fig. 5B) indicates that the characteristic peaks related to the MB C–H groups are observed at 770 cm^{-1} and 1154 cm^{-1} .⁴¹ The band at 1625 cm^{-1} reflects the stretching of the C–C bonds of the MB's aromatic rings. The

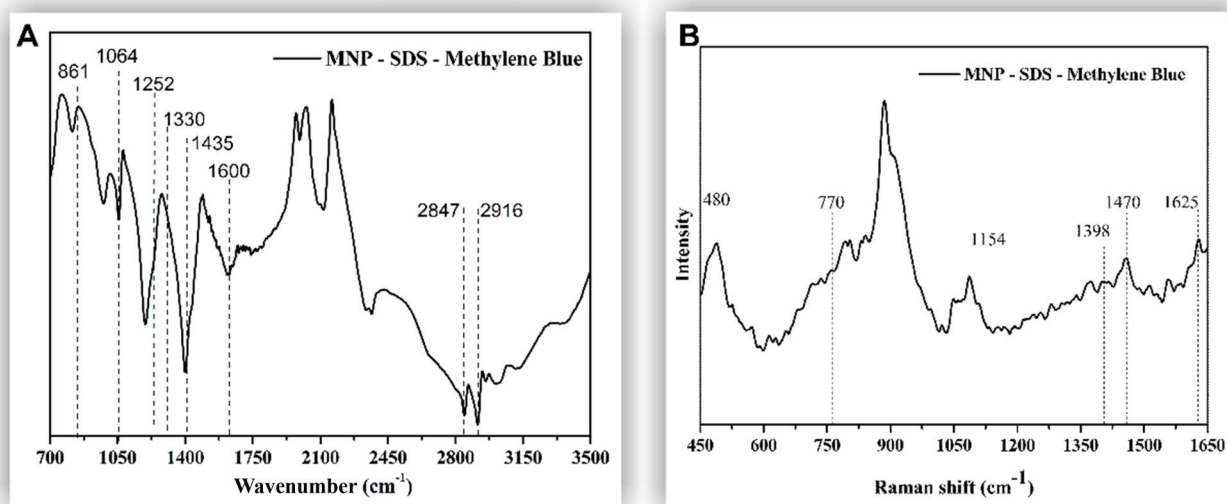


Fig. 5 FTIR (A) and Raman (B) spectra of MNP-SDS–methylene blue.



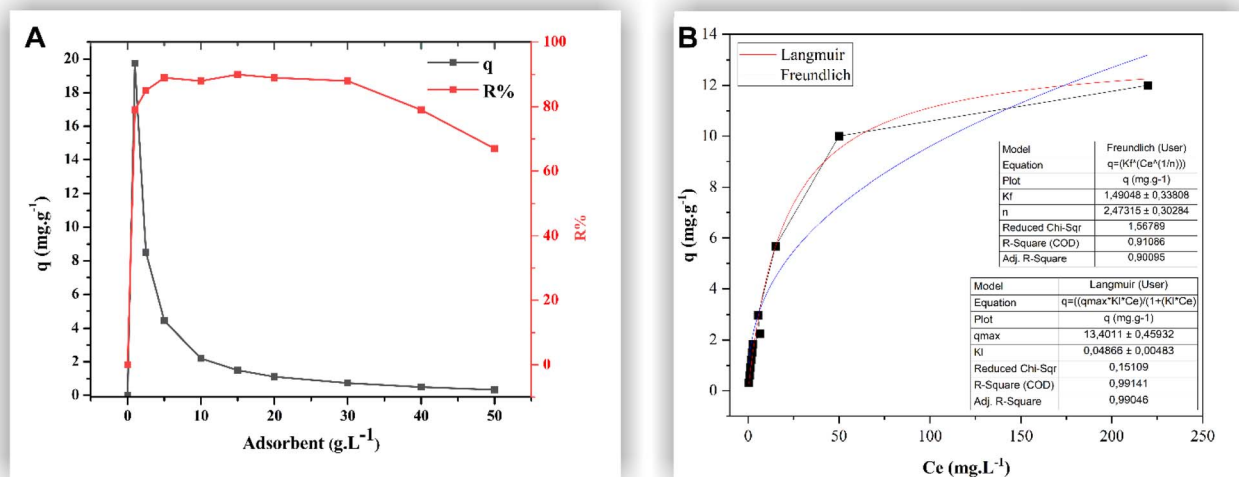


Fig. 6 Influence of MNP-SDS mass in adsorption process (A); isothermal parameters of the adsorption (B).

bands at 1398 cm⁻¹ and 1470 cm⁻¹ represent vibrations of N-C bonds and CH₃ groups, respectively.⁴²

Influence of adsorbent mass, isothermal, and thermodynamic parameters

Adsorbent mass is a crucial factor in MB removal. A judicious determination of the adsorbent quantity can prevent wastage by avoiding excessive usage without compromising its performance. The highest $R\% = 90\%$ ($q_{\text{exp}} = 1.5$ mg g⁻¹) was obtained using 15 g L⁻¹ of MNP-SDS (Fig. 6A). Higher adsorbent concentrations (≥ 30 g L⁻¹) decreased removal efficiency, probably due to the agglomeration process, which can reduce available sites.⁴³ Regarding removal capacity, the highest q value was obtained by applying 1 g L⁻¹ of adsorbent ($q = 19.75$ mg g⁻¹; $R\% = 79\%$). From then onwards, the q value dropped sharply, attributed to the increase in adsorbent mass; however, the $R\%$ parameter did not increase proportionally. Therefore, we opted to use the adsorbent mass that resulted in

the highest $R\%$ value for both isothermal and thermodynamic experiments, that is, 15 g L⁻¹ of MNP-SDS. The results obtained are deemed satisfactory when compared to existing literature. For instance, Yimin *et al.* utilized HA-Fe₃O₄ for MB removal and achieved a removal capacity of 0.291 mmol g⁻¹.⁴⁴ On the other hand, Zhang *et al.* achieved a higher value ($q_{\text{exp}} = 28$ mg g⁻¹) using humic acid-coated Fe₃O₄ nanoparticles, surpassing the removal capacity of the previously mentioned adsorbent.⁴⁵ Nevertheless, it is important to consider other factors, such as cost and system structure, to ascertain the applicability of the adsorbent.

The isothermal parameters of the adsorption are important not only to identify the affinity level between adsorbent/adsorbate but also to investigate adsorption equilibrium, *i.e.*, when adsorption and desorption occur at the same rate. In Fig. 6B, a favorable isothermal shape is evident, indicating a high adsorbate mass retained per unit mass for a low equilibrium concentration of adsorbate in the liquid phase.⁴⁶ The

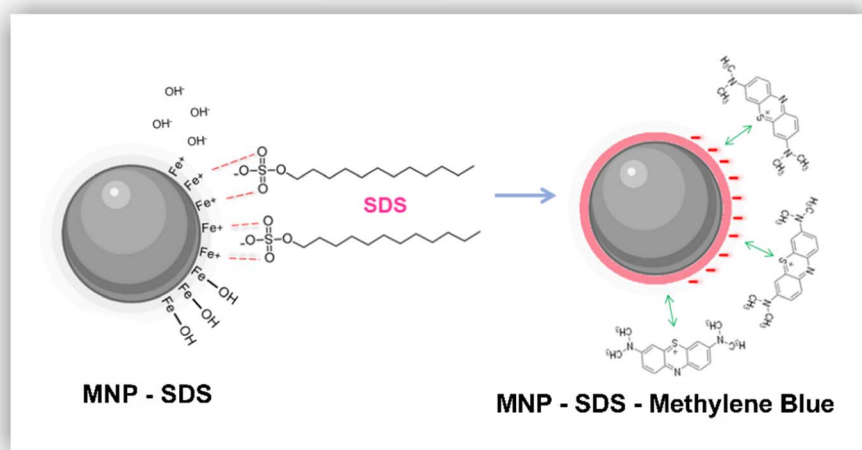


Fig. 7 Adsorption mechanism between MNP-SDS and MB dye.



model that best fit the data was the Langmuir model, with $R^2 = 0.9914$. This model assumes the existence of a defined range of available sites, equivalent energy, and monolayer adsorption, with dye molecules not interacting with each other. Thus, each available site admits only one molecule, unlike the Freundlich model, in which adsorption would take place in a heterogeneous surface and multilayers.⁴⁶

The Gibbs free energy, calculated based on eqn (3), resulted in $-5.45 \text{ kJ mol}^{-1}$. The negative ΔG indicates that energy is being released in the process, which translates into a spontaneous, favorable reaction.^{46,47} Based on the results obtained here, we propose a possible adsorption mechanism between MNP-SDS and the methylene blue dye (Fig. 7).

During the functionalization process, it is possible that the iron present in the nanoparticles released OH^- into the medium due to a pH elevation induced by the addition of SDS. Subsequently, the positively charged iron present on the surface of the nanoparticles attracted sulphonate groups from SDS, leading to the formation of MNP-SDS nanoparticles. Although the nanoparticles retain a negative charge, functionalization usually reduces the agglomeration phenomenon, rendering binding sites available. Finally, the cationic dye may be attracted by the negative surface charge of MNP-SDS through a monolayer mechanism.

Conclusions

The presence of aquatic contaminants on a molecular scale has become increasingly common in recent years. Among them, dyes stand out by being of difficult retention within wastewater treatment plants. In this study, we investigated the adsorption efficiency of methylene blue in an aqueous solution using Fe_3O_4 nanoparticles functionalized with SDS. Promising results were obtained, as the adsorbent achieved an MB removal percentage of 90% ($q_{\text{exp}} = 1.5 \text{ mg g}^{-1}$). Through factorial experiments we optimized the adsorption process and identified that temperature and time were the most influential variables in this system. Determining the ideal concentration of adsorbent was fundamental to avoid nanoparticle wastage, thus reducing the application costs. The adsorption reaction was spontaneous, favorable, and the data were best fitted to the Langmuir model, indicating adsorption occurs in monolayer. Therefore, we believe that the adsorbent developed here might play a satisfactory role in controlling aquatic pollution by MB.

Data availability

All data generated or analyzed during this study are included in this published article and its ESI.†

Author contributions

JNR and JPO conceived the project. TC and TAS performed the experiments, characterizations, and analysis. TC, ACB, JPO and JNR wrote the paper. STAC, AVFNR, MGP and MCCG revised the writing of the manuscript and data curation. JNR and JPO guided the research.

Conflicts of interest

The authors declare that they have no competing interests.

Acknowledgements

This study used the equipment facilities at the Laboratory of Cellular Ultrastructure Carlos Alberto Redins and LabPetro (UFES, Brazil). Our thanks to both Labs for providing the equipment and technical support for experiments.

References

- 1 A. Badeenezhad, A. Azhdarpoor, S. Bahrami and S. Yousefinejad, *Mol. Simul.*, 2019, **45**, 564–571.
- 2 D. Yimin, Z. Jiaqi, L. Danyang, N. Lanli, Z. Liling, Z. Yi and Z. Xiaohong, *Colloids Surf., A*, 2018, **550**, 90–98.
- 3 M. A. Farghali, M. M. Abo-Aly and T. A. Salaheldin, *Inorg. Chem. Commun.*, 2021, **126**, 108487.
- 4 H. Hosseini, P. Pirahmadi, S. E. Shakeri, E. Khoshbakhti, S. Sharafkhani, V. Fakhri, A. Saeidi, D. J. McClements, W. H. Chen, C.-H. Su and V. Goodarzi, *Int. J. Biol. Macromol.*, 2022, **201**, 133–142.
- 5 S. Ihaddaden, D. Aberkane, A. Boukerroui and D. Robert, *J. Water Proc. Eng.*, 2022, **49**, 102952.
- 6 A. K. H. al jibouri, J. Wu and S. R. Upreti, *J. Water Proc. Eng.*, 2015, **8**, 142–150.
- 7 Z. Hu, C. Guo, P. Wang, R. Guo, X. Liu and Y. Tian, *Chemosphere*, 2022, **305**, 135447.
- 8 G. Shi, C. Ruan, S. He, H. Pan, G. Chen, Y. Ma, H. Dai, X. Chen and X. Yang, *Colloids Surf., A*, 2021, **613**, 126053.
- 9 Z. Lou, Z. Zhou, W. Zhang, X. Zhang, X. Hu, P. Liu and H. Zhang, *J. Taiwan Inst. Chem. Eng.*, 2015, **49**, 199–205.
- 10 Y. Artioli, in *Encyclopedia of Ecology, Five-Volume Set*, Academic Press, 2008, vol. 1–5, pp. 60–65.
- 11 X. Peng, *Sep. Purif. Technol.*, 2024, **350**, 127943.
- 12 L. A. Camacho-Cruz, M. A. Velazco-Medel, A. Cruz-Gómez, G. Cedillo-Valverde and E. Bucio, in *Magnetic Nanoparticles and Polymer Nanocomposites*, ed. I. Khan, M. M. A. Khan and A. Khan, Woodhead Publishing, 2024, pp. 441–458.
- 13 M. Wang and X. You, *Proc. Combust. Inst.*, 2023, **39**, 1157–1164.
- 14 A. S. Alsamani, H. Maher, M. Ghazy, E. S. Ali, A. A. Askalany and B. Baran Saha, *Therm. Sci. Eng. Prog.*, 2024, **49**, 102455.
- 15 S. Lavanya, T. R. Kumar, A. V. Juliet, J. Hakami, I. M. Ashraf and M. Shkir, *Solid State Sci.*, 2022, **128**, 106889.
- 16 G. Jia, J. Guo, Y. Guo, F. Yang and Z. Ma, *Case Stud. Constr. Mater.*, 2024, **20**, e03171.
- 17 A. C. De Lima Barizão, M. F. Silva, M. Andrade, F. C. Brito, R. G. Gomes and R. Bergamasco, *J. Environ. Chem. Eng.*, 2020, **8**, 103618.
- 18 L. Yan, X. Song, J. Miao, Y. Ma, T. Zhao and M. Yin, *J. Water Proc. Eng.*, 2024, **60**, 105215.
- 19 M. G. El-Desouky, A. A. A. Alayyafi, G. A. A. M. Al-Hazmi and A. A. El-Bindary, *J. Mol. Liq.*, 2024, **399**, 124392.
- 20 M. Alsawat, *Int. J. Electrochem. Sci.*, 2024, **19**, 100611.



- 21 P. Zhang, I. Lo, D. O'Connor, S. Pehkonen, H. Cheng and D. Hou, *J. Colloid Interface Sci.*, 2017, **508**, 39–48.
- 22 Y. Y. Xu, M. Zhou, H. J. Geng, J. J. Hao, Q. Q. Ou, S. da Qi, H. L. Chen and X. G. Chen, *Appl. Surf. Sci.*, 2012, **258**, 3897–3902.
- 23 P. Damberg, J. Jarvet and A. J. Gräslund, *Methods Enzymol.*, 2001, **339**, 271–285.
- 24 S. Shariati, M. Faraji, Y. Yamini and A. A. Rajabi, *Desalination*, 2011, **270**, 160–165.
- 25 S. A. Kordkandi and M. Forouzes, *J. Taiwan Inst. Chem. Eng.*, 2014, **45**, 2597–2604.
- 26 C. R. T. Tarley, G. Silveira, W. N. L. dos Santos, G. D. Matos, E. G. P. da Silva, M. A. Bezerra, M. Miró and S. L. C. Ferreira, *Microchem. J.*, 2009, **92**, 58–67.
- 27 C. Silveira, Q. L. Shimabuku, M. Fernandes Silva and R. Bergamasco, *Environ. Technol.*, 2018, **39**, 2926–2936.
- 28 T. T. Nguyen, F. Mammeri and S. Ammar, *Nanomaterials*, 2018, **8**, 149.
- 29 A. Bouafia, S. E. Laouini, A. Khelef, M. L. Tedjani and F. Guemari, *J. Cluster Sci.*, 2021, **32**, 1033–1041.
- 30 L. A. Cobos Cruz, C. A. Martínez Perez, A. M. Villafañe, J. A. Matutes Aquino, J. R. Farias Macilla and P. E. G. Casillas, Influence of Cyclodextrin in the Synthesis of Magnetite, *MRS Online Proc. Libr.*, 2009, **1243**, 11.
- 31 M. Masuku, L. Ouma and A. Pholosi, *Environ. Nanotechnol., Monit. Manage.*, 2021, **15**, 100429.
- 32 B. Stuart, *Infrared Spectroscopy Fundamentals and Applications*, John Wiley & Sons, 2004, vol. 1.
- 33 J. Lin, F. Meng, Y. Zhong, J. Liu, G. Chen, Y. Wan, K. Qian and M. T. Sitaramanjaneya, *J. Mater. Res.*, 2010, **25**, 1992–2000.
- 34 D. Sarahia Guzmán-Hernández, M. Teresa Ramirez-Silva, M. Alberto Romero-Romo, M. A. E. Hafizah, A. F. Riyadi and A. Manaf, *Mater. Sci. Eng.*, 2019, **515**, 012080.
- 35 V. A. J. Silva, P. L. Andrade, M. P. C. Silva, A. D. Bustamante, L. de Los Santos Valladares and J. Albino Aguiar, *J. Magn. Magn. Mater.*, 2013, **343**, 138–143.
- 36 L. Slavov, M. V. Abrashev, T. Merodiiska, C. Gelev, R. E. Vandenberghe, I. Markova-Deneva and I. Nedkov, *J. Magn. Magn. Mater.*, 2010, **322**, 1904–1911.
- 37 D. Han, B. Li, Y. Chen, T. Wu, Y. Kou, X. Xue, L. Chen, Y. Liu and Q. Duan, *Nanotechnology*, 2019, **30**, 465703.
- 38 E. Onoja, S. Chandren, F. I. A. Razak and R. A. Wahab, *J. Biotechnol.*, 2018, **283**, 81–96.
- 39 B. Hao, K. Wang, Y. Zhou, C. Sui, L. Wang, R. Bai and Z. Yang, *ACS Omega*, 2020, **5**, 1109–1119.
- 40 A. A. Alshehri and M. A. Malik, *J. Mater. Sci.: Mater. Electron.*, 2019, **30**, 16156–16173.
- 41 R. R. Naujok, R. V. Duevel and R. M. Corn, *Langmuir*, 1993, **9**, 1771–1774.
- 42 M. R. Shattique and M. Stepanova, *Plasmonics*, 2020, **15**, 427–434.
- 43 T. Wu, G. Yang, J. Cao, Z. Xu and X. Jiang, *Chem. Eng. Res. Des.*, 2022, **188**, 330–341.
- 44 D. Yimin, Z. Jiaqi, L. Danyang, N. Lanli, Z. Liling, Z. Yi and Z. Xiaohong, *Colloids Surf., A*, 2018, **550**, 90–98.
- 45 X. Zhang, P. Zhang, Z. Wu, L. Zhang, G. Zeng and C. Zhou, *Colloids Surf., A*, 2013, **435**, 85–90.
- 46 R. F. Nascimento, A. C. A. Lima, C. B. Vidal, D. Q. Melo and G. S. C. Raulino, *Adsorption: Theoric aspects and environmental applications*, UFC Imprensa Universitária, 2014, vol. 1, p. 256.
- 47 C. J. Cleveland and C. Morris, *Dictionary of Energy*, 2014, pp. 1–680.

